Ferroelectric field effect induced charge carrier transport modulation at quantum dot solar cell heterojunction interface

Yuljae Cho,[a,*] Bo Hou,[b] Paul Giraud,[c] Sangyeon Pak,[d] SeungNam Cha[d,*]

[a]University of Michigan–Shanghai Jiao Tong University Joint Institute, Shanghai Jiao Tong University, 800 Dong Chuan Road, Minhang District, Shanghai 200240, China

Email: yuljae.cho@sjtu.edu.cn

[b]School of Physics and Astronomy, Cardiff University, 5 The Parade, Newport Road, Cardiff, CF24 3AA, United Kingdom

[c]Department of Engineering Science, University of Oxford, Parks Road, Oxford OX1 3PJ, United Kingdom

[d]Department of Physics, Sungkyunkwan University, 2066, Seobu-ro, Jangan-gu, Suwon, Gyeonggi-do, 16419 Republic of Korea

Email: chasn@skku.edu

ABSTRACT

Inherent unidealistic properties associated with materials and device structures inevitably limit performance of photovoltaic devices. To overcome the inherent limit, judicious use of ferroelectric materials has been introduced. Here, we demonstrate modulations of charge carrier transport at the heterojunction interface with respect to polarities of electric dipoles. Attributed to an additional electric field by the ferroelectric effect, a built-in potential at the junction increases, leading to enhanced charge carrier transport, reduced charge recombination, and consequently enhanced power conversion efficiency of lead sulfide quantum dot solar cells. The coupling of the ferroelectric effect with the solar cell provides an important platform to further develop solution processable flat panel solar cell technology.

KEYWORDS

quantum dots, photovoltaics, heterojunction interface, ferroelectric effect, charge carrier dynamics

INTRODUCTION

Coupling of a piezoelectric or ferroelectric effect with semiconductors has attracted tremendous research interest in the fields of electronics and energy in recent years.(1-5) This is because of its ability to overcome inherent limits of materials and/or device structures by inducing an additional electric field that judiciously assists charge transport using the piezoelectric or ferroelectric effect.(4-6) In recent years, we have experienced extreme climate changes due to global warming, significantly impacting our daily lives. To mitigate and resolve this issue, tremendous efforts have been made in emerging solar cell technology. Among various promising solutions, integration of the ferroelectric material into photovoltaic cells has been considered as one of the promising approaches to boost power conversion efficiency (PCE).(6-8)

Colloidal lead sulfide quantum dots (PbS QDs), emerging material for solution-processable photovoltaics, offer a promising platform to realize solution processable, cost-effective, stable, and high-performance photovoltaic devices attributed to their fascinating materials properties, for example, high photostability, bandgap tunability, and high absorption coefficient.(9-11) In addition, the ability to harvest the near-infrared spectrum further provides great advantages for tandem solar cell applications.(12-14) Up to now, several reports have demonstrated a synergistic effect of coupling the piezoelectric effect into PbS QD solar cells (QDSCs).(6,15) For example, a flexible QDSC with the piezoelectric effect showed significant device improvement by inducing the piezoelectric potential/field through stretching and bending the substrate.(6)

However, in terms of flat solar panel applications, it is not practical to use such external stimuli to induce the additional electric field. Therefore, a more practical approach is required when it comes to the photovoltaic applications using the coupling effect on the solid unbendable substrate. In this regard, the ferroelectric effect offers a great advantage to control a direction

of electric dipoles in a desirable way by simply applying an external bias. For this reason, efforts have been paid to investigating the coupling effect between the ferroelectric and photovoltaic effects, for example, in organic and perovskite solar cells.(16-21) However, there has been a lack of systematic researches on the ferroelectric effect in the PbS QDSCs so far due to a small number of crystalline classes available for the ferroelectric effect compatible with PbS QDs, compared to the piezoelectric effect.(22) Furthermore, due to the insulating nature of a large bandgap ferroelectric material, such as poly(vinylidenefluoride-trifluoroethylene) or (P(VDF-TrFE)), coupling of the ferroelectric effect into the PbS QDSCs has been a challenging task to date.(17)

Here, we introduce QDSCs coupled with the ferroelectric effect using the P(VDF-TrFE) island layer to overcome its insulating nature. We demonstrate that the performance of QDSCs is able to be modulated with respect to the direction of electric dipole alignment. In addition, we investigate underlying mechanisms associated with charge carrier dynamics and recombination kinetics induced by the ferroelectric field at the heterojunction interface between an electron transport layer (ETL) and a QD layer. Two sets of systematic simulations are performed and the combined experiment and simulation results demonstrate the modulation of properties at the heterojunction induced by the ferroelectric field effect. This result revealed the relationship between charge carrier dynamics and the associated solar cell parameters concerning the heterojunction interface. We believe that our study on the ferroelectric field-assisted QDSCs offers new revenue for designing optoelectronic devices based on heterojunctions of nanomaterials.

RESULTS AND DISCUSSION

Figure 1(a) illustrates a band diagram of a QDSC composed of indium tin oxide (ITO) as an electrode, a ZnO layer as the ETL, a P(VDF-TrFE) island layer to induce a ferroelectric field,

PbS QD layers, and gold (Au) as a top electrode. Energy band levels of each layer was determined using previous reports.(6,23-29) An inset image in Figure 1(a) shows the chemical structure of P(VDF-TrFE) where the electric dipoles due to negative fluorine and positive hydrogen atom induce an electric field when they are aligned.(30) QDSCs were fabricated by a layer-by-layer (LBL) spin-coating method following our previous reports.(26,31) In particular, an island structure P(VDF-TrFE) layer was introduced in order to ensure charge carrier transport as the P(VDF-TrFE) is a natural insulator.(32-34) The P(VDF-TrFE) island structures could be formed by using two strategies. First, by controlling the concentration of P(VDF-TrFE) solution, we could achieve a P(VDF-TrFE) film with wider channel area to conduct photo-generated charges as shown in Figure S1(a) and (b) in Supporting Information (SI). Second, we employed a spin-casting method, i.e. dropping of the solution while the sample is spinning, to reduce the contact time of the P(VDF-TrFE) solution to the ZnO layer. These strategies led to the formation of P(VDF-TrFE) island structures as shown in Figure S1(c). To form a ferroelectric β-phase, the P(VDF-TrFE) film was thermally annealed in an oven at 130°C for 90 minutes. Figure 1(b) and Figure S2(a) and (b) in SI indicate the P(VDF-TrFE) island structures formed the ferroelectric β-phase.(6,35) Figure 1(c) shows a 3D morphology and phase image of the well-distributed P(VDF-TrFE) island layer measured by atomic force microscopy (AFM), and Figure S2(c) provides the height information of the structure which was found to be ~ 20 nm. Then, PbS QDs were deposited, followed by a ligand exchange process to tune the insulating nature of the QDs capped with oleic acid into N- and P-type semiconducting ones by using tetrabutylammonium iodide (TBAI) and 1,2-ethanedithiol (EDT), respectively. TBAI and EDT ligands were particularly chosen for our study as they have demonstrated high stability with one of the highest performances to date.(36,37) As shown in Figure 1(d), PbS QDs had the bandgap of ~1.43 eV by the ultraviolet-visible spectroscopy (UV-vis) analysis and showed the typical rock-salt cubic crystalline

structure with a lattice fringe of (100) by high-resolution transmission electron microscopy (HRTEM). The total thickness of the QD layers were measured by AFM as shown in Figure S3, and it was found to be approximately 250 and 50 nm for TBAI and EDT layers, respectively.

For simulation work, the similar geometry of the P(VDF-TrFE) islands structure was used. Specifically, a ratio between a ZnO layer (an open area) and the P(VDF-TrFE) island structures was found to be 0.32 – 0.34 (1.7/5 μm) from the AFM image in Figure 1(c). Based on this result, we designed a QDSC simulation model using COMSOL Multiphysics. As shown in Figure 2(a)-(c), the ratio between the ZnO layer and P(VDF-TrFE) island structures was kept to the similar ratio of 0.33 along the y-axis. Solar cell parameters used for simulation studies were from the previous reports using the same ligands and structures.(6,38) From the simulation results, first of all, we noticed the modulation of a depletion region with respect to the polarity of electric dipoles. Compared to the reference model (Figure 2(a)), i.e. the pristine state of electric dipoles, the depletion region was enlarged (Figure 2(b)) when the electric dipoles were aligned in a way that negative charges are positioned toward the ZnO layer and positive charges are positioned toward the QD layer (we denote this as a negative poling from now on). On the contrary, the depletion region was reduced when electric dipoles were aligned to the opposite direction to the negative poling, i.e. positive charges to the ZnO layer and negative charges to the QD layer, as shown in Figure 2(c) (denoted as a positive poling from now on). The modulation of the depletion region is attributed to the ferroelectric field generated by the aligned electric dipoles, and consequently, the built-in potential at the heterojunction interface was modulated, as shown in Figure S4 in SI. Second, the modulation of charge carrier transport induced by the ferroelectric field is visualized in Figure 2(d)-(f) where the direction and the size of arrows indicate an electron flow and the intensity of the electric field at the point. To simulate positive and negative electric poling, charge density at the P(VDF-TrFE)

surface was set from -1.60 to +1.60 mC/m^2 whose values were based on previous reports on the surface charges of poled P(VDF-TrFE) layer.(6,39) As shown in Figure 2(d)-(f) and Figure S5, depending on the polarity of the electric dipoles, electron transport at the heterojunction was modulated. In particular, when the device was positively poled, the QDSCs exhibited enhanced charge carrier transport attributed to the higher electric field at the heterojunction (Figure 2(c) and (f)). This leads to reduced recombination and concomitantly enhanced PCE.

To verify the ferroelectric effect in real QDSCs based on the simulation studies, we fabricated QDSCs with the structure shown in Figure 1(a). It is worth noting that QDSCs with the P(VDF-TrFE) island layer before electric poling (denoted as a reference in Figure 3 and 4) exhibited slightly higher device performance than that of QDSCs without the P(VDF-TrFE) island layer as shown in Figure S6 in SI. This suggests that P(VDF-TrFE) island structures are well-distributed and there is no performance degradation due to the insulating nature of P(VDF-TrFE) polymer. This is due to the spontaneous polarization field of the P(VDF-TrFE) layer and is well-consistent with our previous study using the piezoelectric field.(6) Table S1 summarizes solar cell parameters shown in Figure S6 where average values and standard deviations were extracted from 20 devices for each type using the statistics function in the Origin software. Next, to test the ferroelectric effect on the QDSCs, the electric poling was performed by applying 3 V of DC bias to ITO and Au electrodes for 30 minutes at room temperature, i.e. below the Curie temperature.(40-42) Specifically, applying a positive bias to the ITO and a negative bias to the Au electrodes leads to the dipole polarization shown in Figure 2(b), or negative poling. In contrast, the application of the negative bias to the ITO and the positive bias to the Au electrodes forms the dipole polarization shown in Figure 2(c), or positive poling. After the poling process, the QDSCs were grounded for 2 hours to neutralize any trapped charges. It is also worth noting that after the positive and negative poling processes, the phase

of the P(VDF-TrFE) film did not change as shown in Figure S7, indicating that P(VDF-TrFE) layer is in the ferroelectric β-phase. As shown in Figure 3(a), a dark current level of QDSCs with the negative poling was three orders higher than other QDSCs at low bias voltages, i.e. below the turn-on voltage. The I-V curve at the low bias range is related to shunt current and shunt resistance (R_{sh}), and therefore, the high leakage current indicates that the QDSCs with the negative poling suffered from severe charge carrier loss through recombination.(43-45) This is because as only direction of electric dipoles was changed while maintaining all other conditions, modulation in (photo)current, R_s, and R_{sh}, and consequently recombination losses are correlated to each other. Consequently, the device exhibited the high recombination current, resulting from the lower electric field at the heterojunction by the additional ferroelectric field (negative poling). On the other hand, the QDSCs with the positive poling exhibited the lowest dark current at the low bias voltage and an improved diode curve as the bias increases, which is attributed to the ferroelectric field (positive poling) that enhanced the electric field at the heterojunction. This result suggests that the ferroelectric field can assist effective charge carrier transport, lowering charge recombination rates and thus leakage current. Figure 3(b) illustrates performances of QDSCs with respect to the direction of electric dipoles. Based on the reference cell (black line), overall parameters of the QDSC were significantly improved when the P(VDF-TrFE) island layer was positively poled (red line) whereas the QDSC with the negatively poled P(VDF-TrFE) island layer exhibited poor device performance, in particular, with aggravated FF from 0.58 ± 0.03 to 0.44 ± 0.04, series resistance (R_s) from 5.64 ± 1.67 to 11.44 ± 1.32, and R_{sh} from 221.92 ± 43.72 to 88.35 ± 50.80. The amount of PCE improvement was found to be 60.2 % from negatively poled QDSCs to positively poled QDSCs. Interestingly, the QDSC with the negative poling returned to its original performance when the positive poling was performed to the negatively poled device subsequently, depicted with a green line in Figure 3(b). In contrast, QDSCs with only ZnO layer did not exhibit any

photocurrent modulation as shown in Figure S8 in SI, suggesting that the charge modulation is due to the ferroelectric field/potential by the P(VDF-TrFE) island structures. Key parameters of the QDSCs are shown in Table S2 and statistics of device performance are summarized in Figure 3(c), (d), and Table 1. In order to demonstrate that the modulation of QDSC performance was sorely from the ferroelectric effect, we compared the QDSCs with a non-ferroelectric layer and the QDSCs with the P(VDF-TrFE) layer. As shown in Figure S9 and Table S4 in SI, the QDSCs with the non-ferroelectric layer did not exhibit performance modulations when the devices were positively and negatively poled. Furthermore, changes in FF values were noticeable in the QDSCs with the P(VDF-TrFE) layer where the FF values increase (or decrease) to 0.58 (or 0.44) when the QDSC was positively (or negatively) poled. On the contrary, there were no significant changes in FF values in the QDSCs with the non-ferroelectric layer. This further supports the coupling of the ferroelectric and photovoltaic effects in QDSCs with the P(VDF-TrFE) island layer. The experiment results further demonstrated improved QDSC performance by the positive poling which enhanced electric field at the heterojunction. This led to efficient charge carrier transport and reduced charge recombination, consistent with the simulation data in Figure 2.

To further gain an insight into the pivotal role of the ferroelectric effect on the QDSC performance, we carried out further device simulation using COMSOL Multiphysics and SCAPS. First, we compared the ratio between J_{SC} of the reference QDSCs (denoted as J_{SC0}) and J_{SC} of the QDSCs extracted by COMSOL simulation using the model studied in Figure 2. As shown in Figure 4(a) and (b), both the experiment and COMSOL simulation results show a similar trend. As the polarity of electric dipoles changed from negative to positive, the J_{SC}/J_{SC0} ratio increased. This suggests that more charges were collected at the electrode in QDSCs with the positive poling, which is well consistent with the simulation result discussed in Figure 2(d)-

(f). Second, another set of device simulation was carried out using SCAPS. In this simulation setting, we used QDSC parameters attained from experiment results (Table 1) whereas the ferroelectric material was not constructed in the QDSC structure. Therefore, the simulation result will provide the relationship between the ferroelectric effect in the QDSC and the corresponding parameter modulations due to the ferroelectric effect. As shown in Figure 4(a) and (c), we observed a similar trend that the J_{SC}/J_{SC0} ratio increased using parameters from the experiment results. This again indicates that more charges were collected at the electrode because of enhanced electric field at the heterojunction (Figure 4(a)) and reduced R_s as well as increased R_{sh} (Figure 4(c)), demonstrating the coupling effect of the ferroelectric effect with QDSC parameters associated with the charge carrier dynamics. From the combined results of experiments and both simulations, we concluded two primary effects of the ferroelectric field at the heterojunction interface. First, the ferroelectric effect effectively modulated charge carrier transport at the heterojunction. In particular, with the positive poling, more photogenerated charges were collected at the electrode attributed to the facilitated charge carrier transport and reduced recombination at the heterojunction, which is consistent with the Figure 2 and 3. Second, the SCAPS device simulation further demonstrated the relationship between the ferroelectric effect and the corresponding modulation of QDSC parameters. Facilitated charge carrier transport is projected to the decrease in the R_s value whereas reduced recombination is projected to the increase in the R_{sh} value when the device was positively poled.(43-45) On the contrary, with the negative poling, QDSCs exhibited aggravated device performance due to inefficient charge carrier transport and increase in recombination, which was projected to the device parameters (R_s and R_{sh}) and demonstrated by the device simulation.

CONCLUSION

In sum, we investigated the role of the ferroelectric effect at the heterojunction interface between the ZnO and the QD layer and corresponding changes in QDSC parameters. Through the electric poling processes, the polarity of P(VDF-TrFE) layer was able to be tuned, leading to the modulation of charge carrier dynamics and recombination kinetics of the QDSCs. With the positive poling, a higher built-in potential was induced at the heterojunction, resulting in an increase in photocurrent due to efficient charge transport and reduced recombination. On the other hand, QDSCs with the negative poling exhibited a high leakage current in the dark, indicating high recombination at the heterojunction due to the reduced built-in potential. The results were supported by both experiment and two sets of simulation studies using COMSOL Multiphysics and SCAPS. Our study provides valuable information on the effect of the ferroelectric field on the QDSC performance, and the relationship between the ferroelectric effect and corresponding modulation of QDSC parameters.

ASSOCIATED CONTENT

Supporting Information. The supporting Information is available free of charge.

Details of experiment methods and simulation modeling parameters, Characterization of P(VDF-TrFE) island layer using AFM, FTIR, and XRD, Details of COMSOL simulation results on electric field and charge carrier transport modulation at the heterojunction interface, QDSCs experiment data are provided.

AUTHOR INFORMATION

Corresponding Author

*Email: yuljae.cho@sjtu.edu.cn (Y.C.)

*Email: chasn@skku.edu (S.C.)

Author Contributions

Y.C. performed device fabrications and device characterization. B.H. synthesized materials and performed materials characterization. P.G. carried out the simulation work. S.P. performed Atomic Force Microscopy analysis. The manuscript was written by Y.C. together with S.C. and revised by all authors. All authors have given approval to the final version of the manuscript.

Notes

The authors declare no competing financial interest.

ACKNOWLEDGMENT

This work was financially supported by the National Natural Science Foundation of China, grant number 52050410331. Y.C. would like to thank University of Michigan–Shanghai Jiao Tong University Joint Institution for a support of this work.

REFERENCES

1. Wang, L.; Liu, S.; Feng, X.; Xu, Q.; Bai, S.; Zhu, L.; Chen, L.; Qin, Y.; Wang, Z.L. Ultrasensitive vertical piezotronic transistor based on ZnO twin nanoplatelet. *ACS nano* **2017**, *11*(5), 4859-4865.

2. Zhu, J.; Zhou, X.; Jing, L.; Hua, Q.; Hu, W.; Wang, Z.L., Piezotronic effect modulated flexible AlGaN/GaN high-electron-mobility transistors. *ACS nano* **2019**, *13*(11), 13161-13168.

3. An, C.; Qi, H.; Wang, L.; Fu, X.; Wang, A.; Wang, Z.L.; Liu, J. Piezotronic and piezo-phototronic effects of atomically-thin ZnO nanosheets. *Nano Energy* **2021**, *82*, 105653.

4. Cho, Y.; Pak, S.; An, G.H.; Hou, B.; Cha, S. Quantum Dots for Hybrid Energy Harvesting: From Integration to Piezo-Phototronics. *Isr. J. Chem.* **2019**, *59*(8), 747-761.

5. Zhang, Y.; Jie, W.; Chen, P.; Liu, W.; Hao, J. Ferroelectric and piezoelectric effects on the optical process in advanced materials and devices. *Adv. Mater.* **2018**, *30*(34), 1707007.

6. Cho, Y.; Giraud, P.; Hou, B.; Lee, Y.W.; Hong, J.; Lee, S.; Pak, S.; Lee, J.; Jang, J.E.; Morris, S.M.; Sohn, J.I.; Cha, S.; Kim, J.M. Charge transport modulation of a flexible quantum dot solar cell using a piezoelectric effect. *Adv. Energy Mater.* **2018**, *8*(3), 1700809.

7. Zhang, Y.; Yang, Y.; Wang, Z.L. Piezo-phototronics effect on nano/microwire solar cells. *Energy Environ. Sci.* **2012**, *5*(5), 6850-6856.

8. Zheng, D.Q.; Zhao, Z.; Huang, R.; Nie, J.; Li, L.; Zhang, Y. High-performance piezo-phototronic solar cell based on two-dimensional materials. *Nano Energy* **2017**, *32*, 448-453.

9. Liu, M.; Voznyy, O.; Sabatini, R.; De Arquer, F.P.G.; Munir, R.; Balawi, A.H.; Lan, X.; Fan, F.; Walters, G.; Kirmani, A.R.; Hoogland, S.; Laquai, F.; Amassian, A.; Sargent, E.H. Hybrid organic–inorganic inks flatten the energy landscape in colloidal quantum dot solids. *Nat. Mater.* **2017**, *16*(2), 258-263.

10. Xue, Y.; Yang, F.; Yuan, J.; Zhang, Y.; Gu, M.; Xu, Y.; Ling, X.; Wang, Y.; Li, F.; Zhai, T.; Li, J.; Cui, C.; Chen, Y.; Ma, W. Toward scalable PbS quantum dot solar cells using a tailored polymeric hole conductor. *ACS Energy Lett*. **2019**, *4*(12), 2850-2858.

11. Shi, G.; Kaewprajak, A.; Ling, X.; Hayakawa, A.; Zhou, S.; Song, B.; Kang, Y.; Hayashi, T.; Altun, M.E.; Nakaya, M.; Liu, Z.; Wang, H.; Sagawa, T.; Ma, W. Finely interpenetrating bulk heterojunction structure for lead sulfide colloidal quantum dot solar cells by convective assembly. *ACS Energy Lett*. **2019**, *4*(4), 960-967.

12. Sun, B.; Johnston, A.; Xu, C.; Wei, M.; Huang, Z.; Jiang, Z.; Zhou, H.; Gao, Y.; Dong, Y.; Ouellette, O.; Zheng, X.; Liu, J.; Choi, M.J.; Guo, Y.; Baek, S.W., Laquai, F.; Bakr, O.M.; Ban, D.; Voznyy, O.; de Arquer, F.P.G.; Sargent, E.H. Monolayer perovskite bridges enable strong quantum dot coupling for efficient solar cells. *Joule* **2020**, *4*(7), 1542-1556.

13. Baek, S.W.; Jun, S.; Kim, B.; Proppe, A.H.; Ouellette, O.; Voznyy, O.; Kim, C.; Kim, J.; Walters, G.; Song, J.H.; Jeong, S.; Byun, H.R.; Jeong, M.S.; Hoogland, S.; de Arquer, F.P.G.; Kelley, S.O.; Lee, J.Y.; Sargent, E.H. Efficient hybrid colloidal quantum dot/organic solar cells mediated by near-infrared sensitizing small molecules. *Nat. Energy* **2019**, *4*(11), 969-976.

14. Liu, M.; Che, F.; Sun, B.; Voznyy, O.; Proppe, A.; Munir, R.; Wei, M.; Quintero-Bermudez, R.; Hu, L.; Hoogland, S.; Mandelis, A.; Amassian, A.; Kelley, S.O.; de Arquer, F.P.G.; Sargent, E.H. Controlled steric hindrance enables efficient ligand exchange for stable, infrared-bandgap quantum dot inks. *ACS Energy Lett*. **2019**, *4*(6), 1225-1230.

15. Shi, J.; Zhao, P.; Wang, X. Piezoelectric-polarization-enhanced photovoltaic performance in depleted-heterojunction quantum-dot solar cells. *Adv. Mater*. **2013**, *25*(6), 916-921.

16. Nalwa, K. S.; Carr, J. A.; Mahadevapuram, R. C.; Kodali, H. K.; Bose, S.; Chen, Y.; Petrich, J. W.; Ganapathysubramanian, B.; Chaudhary, S. Enhanced charge separation in organic photovoltaic films doped with ferroelectric dipoles. *Energy Environ. Sci.*, **2012**, *5(5)*, 7042-7049

17. Jia, E.; Wei, D.; Cui, P.; Ji, J.; Huang, H.; Jiang, H.; Dou, S.; Li, M.; Zhou, C.; Wang, W. Efficiency Enhancement with the Ferroelectric Coupling Effect Using P(VDF-TrFE) in $CH_3NH_3PbI_3$ Solar Cells. *Adv*. *Sci*. **2019**, *6*(16), 1900252.

18. Yuan, Y.; Reece, T. J.; Sharma, P.; Poddar, S.; Ducharme, S.; Gruverman, A.; Yang, Y.; Huang, J. Efficiency enhancement in organic solar cells with ferroelectric polymers. *Nat. Mater.* **2011**, *10*, 296–302.

19. Yang, B.; Yuan, Y.; Sharma, P.; Poddar, S.; Korlacki, R.; Ducharme, S.; Gruverman, A.; Saraf, R.; Huang, J. Tuning the Energy Level Offset between Donor and Acceptor with Ferroelectric Dipole Layers for Increased Efficiency in Bilayer Organic Photovoltaic Cells. *Adv. Mater.* **2012**, *24(11)*, 1455-1460.

20. Jo, S. B.; Kim, M.; Sin, D. H.; Lee, J.; Kim, H. G.; Ko, H.; Cho, K. Carrier-Selectivity-Dependent Charge Recombination Dynamics in Organic Photovoltaic Cells with a Ferroelectric Blend Interlayer. *Adv. Energy Mater.* **2015**, *5(19)*, 1500802.

21. Xiao, Z.; Dong, Q.; Sharma, P.; Yuan, Y.; Mao, B.; Tian, W.; Gruverman, A.; Huang, J. Synthesis and Application of Ferroelectric P(VDF-TrFE) Nanoparticles in Organic Photovoltaic Devices for High Efficiency. *Adv. Energy Mater.* **2013**, *3(12)*, 1581-1588.

22. Bowen, C.R.; Kim, H.A.; Weaver, P.M.; Dunn, S. Piezoelectric and ferroelectric materials and structures for energy harvesting applications. *Energy Environ*. *Sci*. **2014**, *7*(1), 25-44.

23. Hou, B.; Cho, Y.; Kim, B. S.; Hong, J.; Park, J. B.; Ahn, S. J.; Sohn, J. I.; Cha, S.; Kim, J. M. Highly Monodispersed PbS Quantum Dots for Outstanding Cascaded-Junction Solar Cells. *ACS Energy Lett.* **2016**, *1*(4), 834-839.

24. Cho, Y.; Lee, S.; Hong, J.; Pak, S.; Hou, B.; Lee, Y. -W.; Jang, J. E.; Im, H.; Sohn, J. I. Cha, S.; Kim, J. M. Sustainable hybrid energy harvester based on air stable quantum dot solar cells and triboelectric nanogenerator, *J. Mater. Chem. A* **2018**, *6*(26), 12440-12446.

25. Hou, B.; Cho, Y.; Kim, B. -S.; Ahn, D.; Lee, S.; Park, J. B.; Lee, Y. -W.; Hong, J.; Im, H.; Morris, S. M.; Sohn, J. I.; Cha, S.; Kim, J. M. Red green blue emissive lead sulfide quantum dots: heterogeneous synthesis and applications. *J. Mater. Chem. C* **2017**, *5*(15), 3692-3698.

26. Cho, Y.; Hou, B.; Lim, J.; Lee, S.; Pak, S.; Hong, J.; Giraud, P.; Jang, A.R.; Lee, Y.W.; Lee, J.; Jang, J.E.; Snaith, H.J.; Morris, S.M.; Sohn, J.I.; Cha, S.; Kim, J.M. Balancing charge carrier transport in a quantum dot p–n junction toward hysteresis-free high-performance solar cells. *ACS Energy Lett*. **2018**, *3*(4), 1036-1043.

27. Chuang, C. -H. M.; Brown, P. R.; Bulović, V.; Bawendi, M. G. Improved performance and stability in quantum dot solar cells through band alignment engineering. *Nat. Mater.* **2014**, *13*, 796-801.

28. Chuang, C. -H. M.; Maurano, A.; Brandt, R. E.; Hwang, G. W.; Jean, J.; Buonassisi, T.; Bulović, V.; Bawendi, M. G. Open-Circuit Voltage Deficit, Radiative Sub-Bandgap States, and Prospects in Quantum Dot Solar Cells. *Nano Lett.* **2015**, *15*(5), 3286–3294.

29. Liu, M.; García de Arquer, F. P.; Li, Y.; Lan, X.; Kim, G. -H.; Voznyy, O.; Jagadamma, L. K.; Abbas, A. S.; Hoodgland, S.; Lu, Z.; Kim, J. Y.; Amassian, A.; Sargent, E. H. Double-Sided Junctions Enable High-Performance Colloidal-Quantum-Dot Photovoltaics. *Adv. Mater.* **2016**, *28*(21), 4142-4148.

30. Cho, Y.; Park, J.B.; Kim, B.S.; Lee, J.; Hong, W.K.; Park, I.K.; Jang, J.E.; Sohn, J.I.; Cha, S.; Kim, J.M. Enhanced energy harvesting based on surface morphology engineering of P (VDF-TrFE) film. *Nano Energy* **2015**, *16*, 524-532.

31. Hou, B.; Kim, B.S.; Lee, H.K.H.; Cho, Y.; Giraud, P.; Liu, M.; Zhang, J.; Davies, M.L.; Durrant, J.R.; Tsoi, W.C.; Li, Z.; Dimitrov, S.D.; Sohn, J.I.; Cha, S.; Kim, J.M. Multiphoton Absorption Stimulated Metal Chalcogenide Quantum Dot Solar Cells under Ambient and Concentrated Irradiance. *Adv*. *Funct*. *Mater*. **2020**, *30*(39), 2004563.

32. Yang, B.; Yuan, Y.; Sharma, P.; Poddar, S.; Korlacki, R.; Ducharme, S.; Gruverman, A.; Saraf, R.; Huang, J. Tuning the Energy Level Offset between Donor and Acceptor with Ferroelectric Dipole Layers for Increased Efficiency in Bilayer Organic Photovoltaic Cells. *Adv. Mater.* **2012**, *24*(11), 1455-1460.

33. Choi, Y. -Y.; Yun, T. G.; Qaiser, N.; Paik, H.; Roh, H. S.; Hong, J.; Hong, S.; Han, S. M.; No, K. Vertically aligned P(VDF-TrFE) core-shell structures on flexible pillar arrays. *Sci. Rep.* **2015**, 5, 10728.

34. Cho, Y.; Pak, S.; Li, B.; Hou, B.; Cha, S. Enhanced Direct White Light Emission Efficiency in Quantum Dot Light-Emitting Diodes via Embedded Ferroelectric Islands Structure. *Adv. Funct. Mater.* **2020**, 2104239.

35. Mao, D.; Quevedo-Lopez, M.A.; Stiegler, H.; Gnade, B.E.; Alshareef, H.N. Optimization of poly (vinylidene fluoride-trifluoroethylene) films as non-volatile memory for flexible electronics. *Org. Electron.* **2010**, *11*(5), 925-932.

36. Chuang, C.H.M.; Brown, P.R.; Bulović, V.; Bawendi, M.G. Improved performance and stability in quantum dot solar cells through band alignment engineering. *Nat. Mater.* **2014**, *13*(8), 796-801.

37. Hu, L.; Lei, Q.; Guan, X.; Patterson, R.; Yuan, J.; Lin, C.H.; Kim, J.; Geng, X.; Younis, A.; Wu, X.; Liu, X.; Wan, T.; Chu, D.; Wu, T.; Huang, S. Optimizing Surface Chemistry of PbS Colloidal Quantum Dot for Highly Efficient and Stable Solar Cells via Chemical Binding. *Adv. Sci.* **2021**, *8*(2), 2003138.

38. Lan, X.; Voznyy, O.; Kiani, A.; García de Arquer, F. P.; Abbas, A. S.; Kim, G. -H.; Liu, M.; Yang, Z.; Walters, G.; Xu, J.; Yuan, M.; Ning, Z.; Fan, F.; Kanjanaboos, P.; Kramer, I.; Zhitomirsky, D.; Lee, P.; Perelgut, A.; Hoogland, S.; Sargent, E. H.; Passivation Using Molecular Halides Increases Quantum Dot Solar Cell Performance. *Adv. Mater.* **2016**, *28*(2), 299-304.

39. Lee, K.Y.; Kim, S.K.; Lee, J.H.; Seol, D.; Gupta, M.K.; Kim, Y.; Kim, S.W. Controllable charge transfer by ferroelectric polarization mediated triboelectricity. *Adv. Funct. Mater.* **2016**, *26*(18), 3067-3073.

40. Kim, J.; Lee, J. H.; Ryu, H.; Lee, J. -H.; Khan, U.; Kim, H.; Kwak, S. S.; Kim, S. -W. High-Performance Piezoelectric, Pyroelectric, and Triboelectric Nanogenerators Based on P(VDF-TrFE) with Controlled Crystallinity and Dipole Alignment. *Adv. Funct. Mater.* **2017**, *27*(22), 1700702.

41. Lee, J. -H.; Hinchet, R.; Kim, T. Y.; Ryu, H.; Seung, W.; Yoon, H. -J.; Kim, S. -W. Control of Skin Potential by Triboelectrification with Ferroelectric Polymers. *Adv. Mater.* **2015**, *27*(37), 5553-5558.

42. Lee, K. Y.; Kim, S. K.; Lee, J. -H.; Seol, D.; Gupta, M. K.; Kim, Y.; Kim, S. -W. Controllable Charge Transfer by Ferroelectric Polarization Mediated Triboelectricity. *Adv. Funct. Mater.* **2016**, *26*(18), 3067-3073.

43. Kim, J.; Choi, H.; Nahm, C.; Moon, J.; Kim, C.; Nam, S.; Jung, D.R.; Park, B. The effect of a blocking layer on the photovoltaic performance in CdS quantum-dot-sensitized solar cells. *J. Power Sources* **2011**, *196*(23), 10526-10531.

44. Ding, C.; Zhang, Y.; Liu, F.; Kitabatake, Y.; Hayase, S.; Toyoda, T.; Wang, R.; Yoshino, K.; Minemoto, T.; Shen, Q. Understanding charge transfer and recombination by interface engineering for improving the efficiency of PbS quantum dot solar cells. *Nanoscale Horiz.* **2018**, *3*(4), 417-429.

45. Servaites, J.D.; Ratner, M.A.; Marks, T.J. Organic solar cells: A new look at traditional models. *Energy Environ. Sci.* **2011**, *4*(11), 4410-4422.

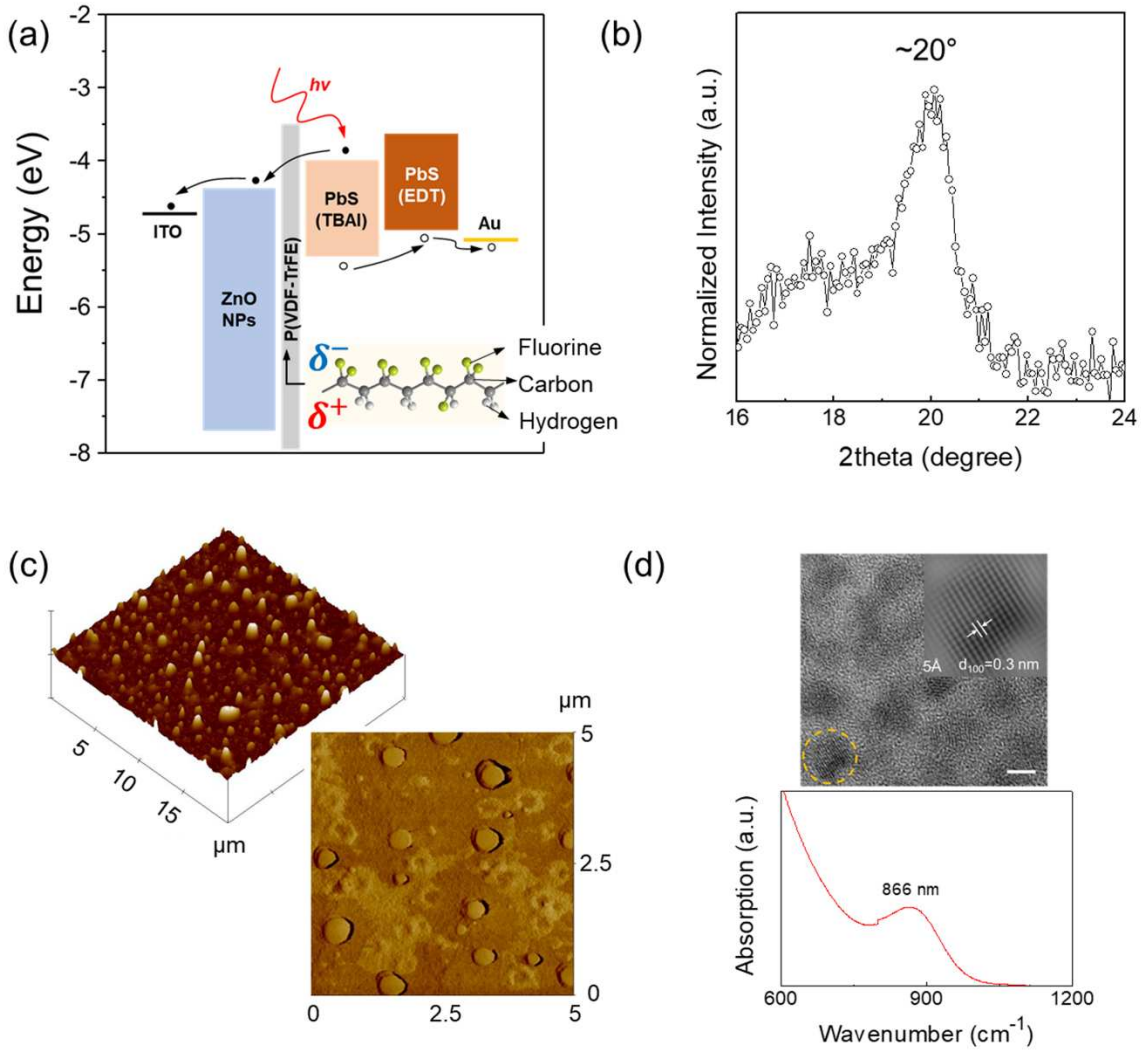

Figure 1. (a) The structure of the QDSC with the ferroelectric P(VDF-TrFE) island layer where the inset image shows the chemical structure of the P(VDF-TrFE). (b) XRD measurement P(VDF-TrFE) island structures coated on a glass substrate. (c) 3D and phase image of the P(VDF-TrFE) island layer after the thermal annealing measured by AFM. (d) HRTEM image and optical absorption spectrum of the as-synthesized PbS QDs (Scale bar: 4 nm).

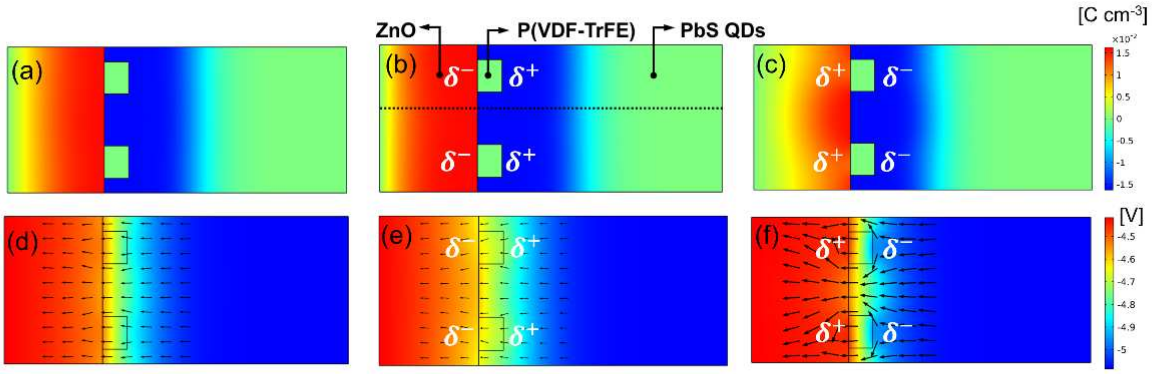

Figure 2. (a)-(c) Modulation of the depletion region with respect to the direction of the electric dipole alignment: (a) initial state, (b) negatively poled, and (c) positively poled where the negative and positive charges in the image indicate the direction of electric dipoles. (d)-(f) Visualized electron flows and electric field intensity depicted by the direction and size of arrows, respectively: (d) initial state, (e) negatively poled, and (f) positively poled where the negative and positive charges in the image indicate the direction of electric dipoles.

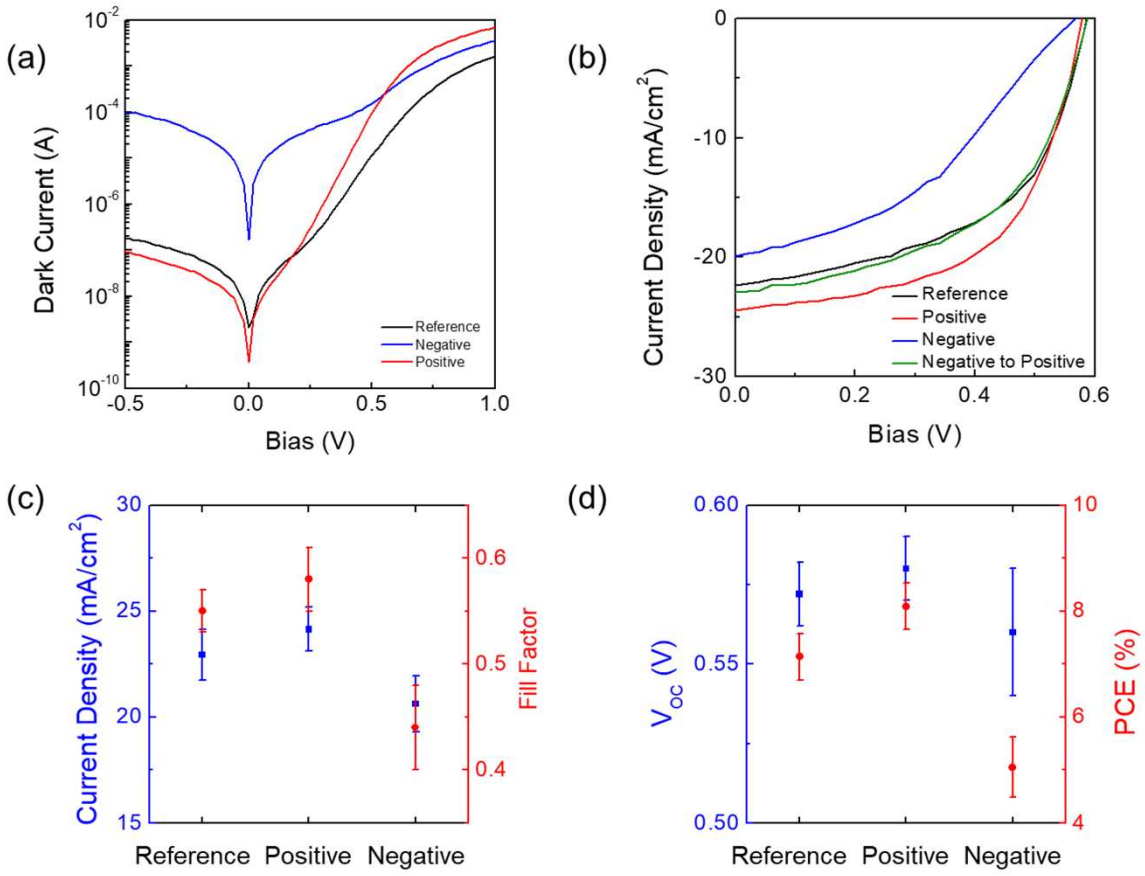

Figure 3. (a) Dark current and (b) photocurrent of reference, negatively poled, and positively poled QDSCs. (c) and (d) Parameters of reference, negatively poled, and positively poled QDSCs.

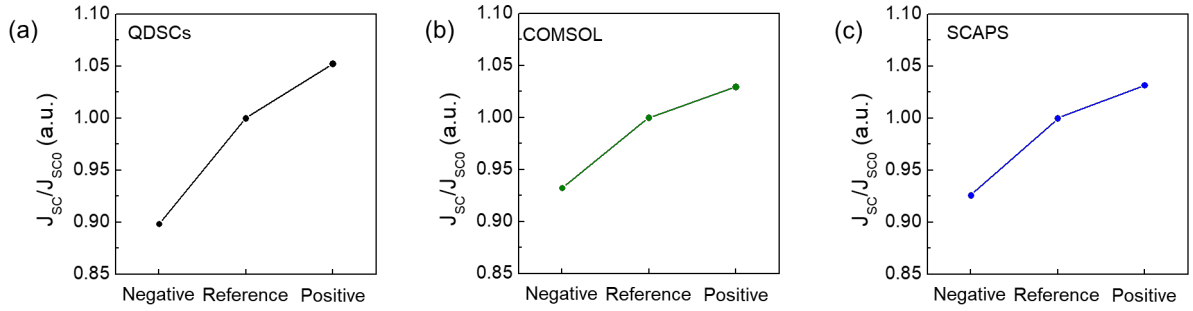

Figure 4. (a)-(c) The ratio of J_{SC}/J_{SC0} in QDSCs with respect to the direction of electric poling extracted from (a) real QDSC devices, (b) COMSOL simulation, and (c) SCAPS simulation.

Table 1. Average QDSC performances with respect to the poling direction.

	V_{OC} (V)	J_{SC} (mAcm^{-2})	R_s (Ωcm^2)	R_{sh} (Ωcm^2)	FF	PCE (%)
Negative	0.56 ± 0.01	20.61 ± 1.32	11.44 ± 1.32	88.35 ± 50.80	0.44 ± 0.04	5.05 ± 0.57
Reference	0.57 ± 0.01	22.94 ± 1.21	9.04 ± 0.62	205.92 ± 39.22	0.55 ± 0.02	7.14 ± 0.33
Positive	0.58 ± 0.02	24.14 ± 1.04	5.64 ± 1.67	221.92 ± 43.72	0.58 ± 0.03	8.09 ± 0.44

1 TABLE OF CONTENTS

2